

Sheared two-dimensional radiofrequency excitation for off-resonance robustness and fat suppression in reduced field-of-view imaging

Bahadır Alp Barlas^{1,2}  | Cagla Deniz Bahadır^{1,2,3}  | Sevgi Gokce Kafali^{1,2,4}  | Ugur Yilmaz² | Emine Ulku Saritas^{1,2,5} 

¹Department of Electrical and Electronics Engineering, Bilkent University, Ankara, Turkey

²National Magnetic Resonance Research Center (UMRAM), Bilkent University, Ankara, Turkey

³Department of Biomedical Engineering, Cornell University, Ithaca, New York, USA

⁴Department of Bioengineering, University of California Los Angeles, Los Angeles, California, USA

⁵Neuroscience Graduate Program, Bilkent University, Ankara, Turkey

Correspondence

Bahadır Alp Barlas, Electrical and Electronics Engineering, Bilkent University, Ankara TR-06800, Turkey.
Email: barlas@ee.bilkent.edu.tr

Funding information

Türkiye Bilimsel ve Teknolojik Araştırma Kurumu, Grant/Award Number: 117E116

Purpose: Two-dimensional (2D) echo-planar radiofrequency (RF) pulses are widely used for reduced field-of-view (FOV) imaging in applications such as diffusion-weighted imaging. However, long pulse durations render the 2D RF pulses sensitive to off-resonance effects, causing local signal losses in reduced-FOV images. This work aims to achieve off-resonance robustness for 2D RF pulses via a sheared trajectory design.

Theory and Methods: A sheared 2D RF pulse design is proposed to reduce pulse durations while covering identical excitation k-space extent as a standard 2D RF pulse. For a given shear angle, the number of sheared trajectory lines is minimized to obtain the shortest pulse duration, such that the excitation replicas are repositioned outside the slice stack to guarantee unlimited slice coverage. A target fat/water signal ratio of 5% is chosen to achieve robust fat suppression.

Results: Simulations, imaging experiments on a custom head and neck phantom, and in vivo imaging experiments in the spinal cord at 3 T demonstrate that the sheared 2D RF design provides significant improvement in image quality while preserving profile sharpnesses. In regions with high off-resonance effects, the sheared 2D RF pulse improves the signal by more than 50% when compared to the standard 2D RF pulse.

Conclusion: The proposed sheared 2D RF design successfully reduces pulse durations, exhibiting significantly improved through-plane off-resonance robustness, while providing unlimited slice coverage and high fidelity fat suppression. This method will be especially beneficial in regions suffering from a variety of off-resonance effects, such as spinal cord and breast.

KEYWORDS

2D RF pulse, fat suppression, multislice imaging, off-resonance robustness, reduced field-of-view imaging, sheared trajectory

1 | INTRODUCTION

Diffusion-weighted imaging provides a powerful tool for diagnosing conditions related to the pathological changes in tissue microstructure.^{1,2} Although diffusion-weighted

imaging gained its popularity due to its capability of early detection of brain ischemia and cancer,³⁻⁶ it has found a wide range of clinical usage outside the central nervous

system for abdominal tissues and organs such as the breast, prostate, and endometrium.⁷⁻¹¹ Single-shot echo-planar imaging (ssEPI) is by far the most commonly used imaging sequence in diffusion-weighted imaging because of its speed and robustness against motion-induced artifacts, despite the associated off-resonance distortions.^{2,12} Multishot techniques such as readout-segmented EPI,¹³⁻¹⁵ short-axis propeller EPI,¹⁶ and interleaved EPI¹⁷⁻¹⁹ were developed to reduce echo train while keeping the number of shots limited in order to constrain both off-resonance and motion-induced artifacts. In addition, reduced field-of-view (FOV) ssEPI has been proposed to improve in-plane off-resonance robustness by limiting the FOV along the phase-encoding (PE) direction, enabling a significant reduction in the number of PE lines without causing aliasing artifacts.²⁰⁻²³ Applications of reduced-FOV techniques such as outer volume suppression²¹ reinforced with parallel imaging,^{24,25} zonal oblique multislice (ZOOM) EPI,^{26,27} and two-dimensional echo-planar RF (2D RF) pulse excitation^{22,28} together with several combinations of the provided reduced-FOV techniques²⁹ have been demonstrated successfully in various regions. In particular, due to its fat suppression capability and sharp slab profile features,²² reduced-FOV imaging with 2D RF pulse excitation has been widely applied in regions that typically suffer from off-resonance artifacts such as the spinal cord, prostate, and breast.^{6,8,9,30-32}

Despite the improved robustness provided by 2D RF based reduced-FOV ssEPI against in-plane off-resonance distortions, several issues still need to be addressed. Firstly, traversing the excitation k-space in 2D requires longer pulse durations, which in turn increases through-plane off-resonance sensitivity. This sensitivity can cause regions with large susceptibility differences to suffer from a signal loss.²² Furthermore, 2D RF excitations generate replicas along the blipped (i.e., discretely sampled) axis. Assigning the blipped axis as the slice-selection (SS) axis grants important advantages to this technique, such as inherent fat suppression capability and sharp slab profiles. However, as a trade-off, this assignment limits the slice coverage during multislice imaging, since any overlap between the replicas and the prescribed slice stack causes a significant signal loss due to partial saturation effects. While one can adjust the design parameters to extend the distance between the replicas, the resulting 2D RF pulses have even longer durations, further increasing the aforementioned off-resonance sensitivity.²²

One approach to enhance through-plane off-resonance robustness is adaptive 2D RF pulse design using a B_0 field map acquired prior to imaging.³³ Although this technique successfully reduces the off-resonance-based artifacts without compromising from RF pulse performance, the need to obtain an additional B_0 field map and to

redesign a new 2D RF pulse for each subject and each region of interest (ROI) reduces the feasibility of this technique in clinical settings. Another approach is the usage of a second-order shim gradient (Z2) together with a spatial-spectral RF pulse to excite a disk-shaped reduced FOV.^{34,35} While this method achieved a reduction in pulse duration, the low strength of Z2 gradient in commercial MRI systems limits its performance. Previously, two different tilted 2D RF pulse designs were proposed to reposition the replicas along a tilted axis via rotating the excitation k-space trajectory.^{23,36} One of these techniques assigned the blipped axis as the PE-axis, and prioritized pulse duration reduction to enhance off-resonance robustness without considering the fat suppression capability as a criterion.³⁶ The second technique assigned the blipped axis as the SS-axis, providing unlimited slice coverage together with robust fat suppression, without any improvement in off-resonance robustness.²³ This second technique has been successfully applied in various target regions such as the pancreas and prostate.^{37,38}

In this work, we propose a sheared 2D RF pulse design to achieve a significant improvement in through-plane off-resonance robustness by decreasing the pulse duration through a sheared coverage of the excitation k-space. The proposed technique further provides unlimited slice coverage while preserving profile sharpness and fat suppression capability. The sheared and standard 2D RF pulses are compared via extensive simulations, including analyses on pulse duration, profile sharpness, fat suppression capability, and signal comparison under off-resonance effects. In addition, phantom experiments in a custom head and neck phantom and in vivo imaging experiments in the spinal cord at 3T are presented to compare full-FOV ssEPI images and reduced-FOV ssEPI images with the sheared and standard 2D RF pulses. The results show that the sheared 2D RF design achieves reduced pulse durations and high fidelity fat suppression for a wide range of design parameters needed for reduced-FOV imaging, as well as a wide range of scanner hardware limits. Furthermore, the proposed technique accomplishes significant improvement in the off-resonance robustness, demonstrating reduced-FOV images with increased signal levels especially in regions that suffer from high off-resonance effects.

2 | THEORY

2.1 | Standard 2D echo-planar RF pulse design

Standard 2D RF pulses enable independent design of slice profile along SS-axis and slab profile along PE-axis. In this

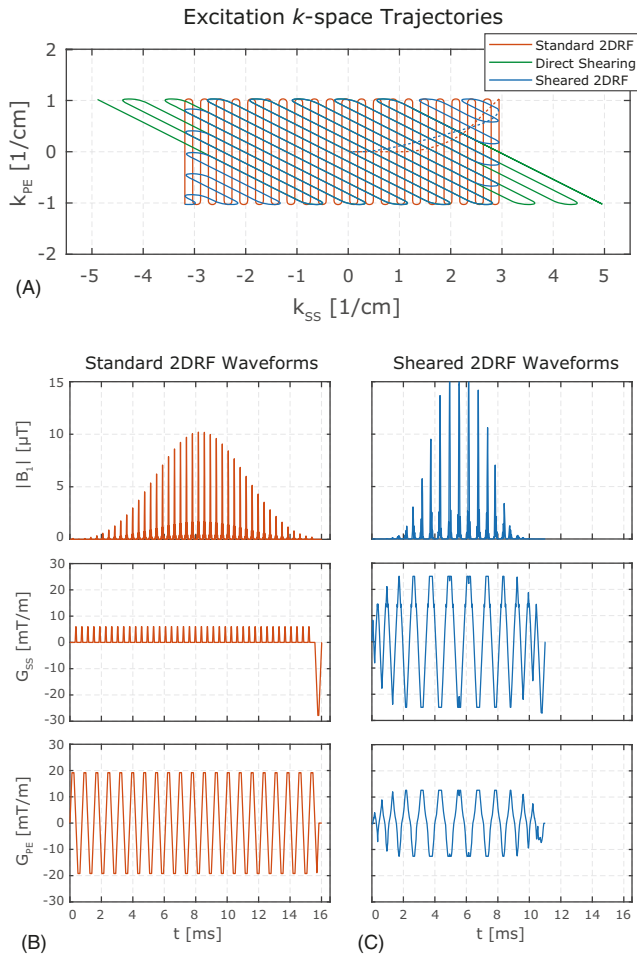


FIGURE 1 The k -space trajectories and radiofrequency (RF)/gradient waveforms for standard and sheared two-dimensional (2D) RF pulses. (A) Excitation k -space trajectories for a standard 2D RF pulse and a sheared 2D RF pulse with $\theta = 63.25^\circ$, reducing N_{blip} from 40 to 14. Direct shearing (green) yields inefficient k -space coverage, whereas the proposed tailoring (blue) achieves identical k -space coverage as the standard 2D RF pulse. The dashed lines correspond to the rephasing gradient lobes during which the RF pulse is off. The RF and gradient waveforms for (B) the standard and (C) the sheared 2D RF pulses, with 16.0 and 11.0 ms pulse durations, respectively. The sheared design enables 31% reduction in pulse duration for this case. For both pulses, VERSE was utilized to minimize pulse durations within the hardware limits. The design parameters were $\text{FOV}_{PE} = 40$ mm, $\Delta z = 4$ mm, $\text{TBW}_{SS} = 3$, and $\text{TBW}_{PE} = 8$. For the standard 2D RF pulse, $N_{\text{max}} = 16$.

work, the fast and blipped directions of the echo-planar k -space trajectory correspond to PE- and SS-axes, respectively (see Figure 1A). The resulting 2D excitation profile features replicas and a relative shift of the fat profile, both along the blipped SS-direction as seen in Figure 2A. In a spin echo sequence, both fat and the replicas can be suppressed using a 180° refocusing RF pulse selective in the SS-axis. Under the small tip angle approximation, a standard 2D RF pulse can be designed as follows:^{39,40}

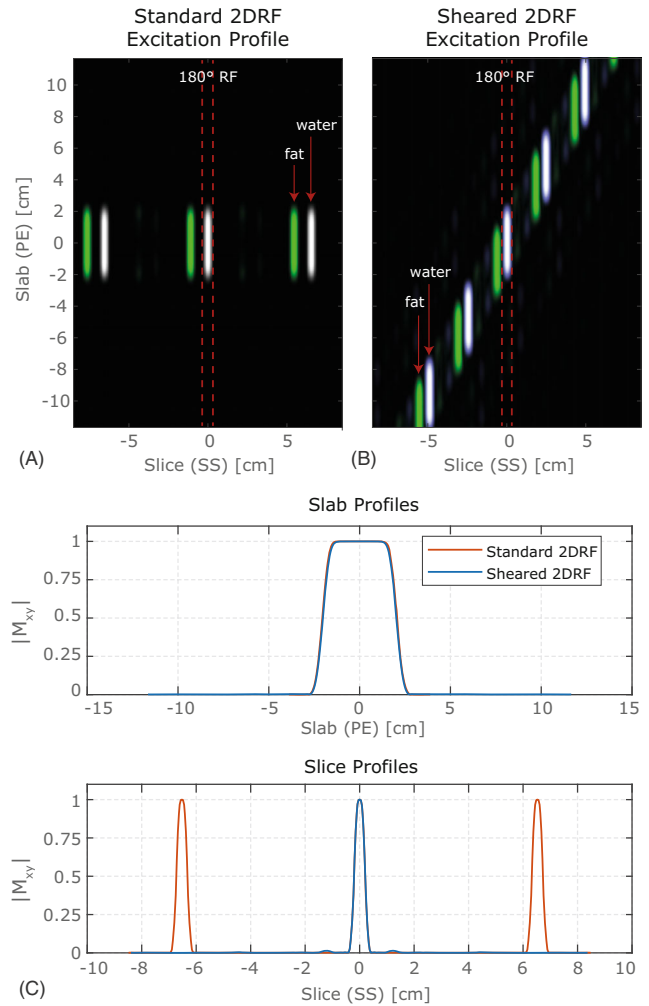


FIGURE 2 The excitation profiles for standard and sheared two-dimensional (2D) radiofrequency (RF) pulses. (A) The 2D excitation profile for the standard 2D RF pulse has replicas along the slice-selection (SS)-axis, limiting the slice coverage to $N_{\text{max}} = 16$. (B) The sheared 2D RF pulse with $\theta = 63.25^\circ$ repositions the replicas along the sheared axis, removing slice coverage limitations. For both 2D RF pulses, both the displaced fat profiles and the replicas can be suppressed using a subsequent 180° refocusing RF pulse that is selective in SS-axis (dashed red lines). (C) One-dimensional central cross-sections of water profiles along phase-encoding and SS-axes demonstrate that the sheared design preserves profile sharpnesses along both axes. The design parameters were identical to those in Figure 1.

$$B_1(t) = C_1(\alpha) W(k_{SS}(t), k_{PE}(t)) \|\mathbf{G}(t)\|_2 \quad (1)$$

Here, $k_{SS}(t)$ and $k_{PE}(t)$ are the SS and PE components of the k -space trajectory, respectively. $C_1(\alpha)$ is a constant that adjusts the flip angle α , W is the excitation k -space weighting to achieve the desired 2D excitation profile, and $\|\mathbf{G}(t)\|_2$ is the ℓ_2 -norm of the gradient vector that scales the RF pulse according to k -space trajectory speed. The profile thicknesses can be calculated as follows:

$$\begin{aligned}\Delta z &= \frac{TBW_{SS}}{K_{SS}} \\ FOV_{PE} &= \frac{TBW_{PE}}{K_{PE}}.\end{aligned}\quad (2)$$

Here, Δz and FOV_{PE} are the slice and slab thicknesses, respectively, and K_{SS} and K_{PE} are the covered k-space extents along the SS- and PE-axes, respectively. Additionally, TBW_{SS} and TBW_{PE} are time-bandwidth products (TBW) describing the slice and slab sharpness, respectively. The separation between the replicas along the SS-direction is:

$$\Delta d_{SS} = \frac{1}{\Delta k_{SS}} = \frac{N_{blip}}{K_{SS}} = \frac{N_{blip}}{TBW_{SS}} \Delta z, \quad (3)$$

where Δk_{SS} is the distance between the consecutive trajectory lines, and N_{blip} is the number of blips in the SS gradient waveform. During a multislice acquisition, any overlap of the targeted slice with the replica profiles of other slices can cause a signal loss due to partial saturation.²³ The maximum number of slices, N_{max} , that can be imaged while avoiding such a signal loss is defined as the number of slices that can fit between two consecutive replicas,²² that is,

$$N_{max} = \frac{\Delta d_{SS}}{\Delta z} = \frac{N_{blip}}{TBW_{SS}}. \quad (4)$$

An increase in N_{max} can be achieved by either increasing N_{blip} or reducing TBW_{SS} , with the trade-offs of increased 2D RF pulse duration or reduced profile sharpness, respectively. Note that this definition of N_{max} assumes infinitely sharp slice profiles, that is, ignores the relatively minor effect of the overlaps between the tails of consecutive slices.²³

As shown in Figure 2A, the chemical shift of fat causes the fat profile to be displaced along the blipped SS-direction. This relative displacement, Δd , is expressed as follows:

$$\Delta d = \frac{T_{fast} \Delta f}{\Delta k_{SS}} = \frac{N_{blip} T_{fast} \Delta f}{TBW_{SS}} \Delta z = \frac{\Delta f}{BW_{SS}} \Delta z. \quad (5)$$

Here, T_{fast} is the duration of each trajectory line and BW_{SS} is the bandwidth along the SS-direction, such that $TBW_{SS} = N_{blip} T_{fast} BW_{SS}$. In addition, Δf is the resonance frequency difference between fat and water. Note that Δd can be quite prominent for 2D RF pulses due to low BW_{SS} . In fact, setting $BW_{SS} \leq \Delta f$ achieves a complete separation of fat and water profiles (i.e., $\Delta d \geq \Delta z$), enabling a subsequent 180° RF pulse to suppress the fat signal.²² While the fat profile is also displaced along the PE-direction, the fast movement in k_{PE} causes this displacement to be negligibly small when compared to FOV_{PE} . In addition,

the displacement in the PE-direction has no effect on fat suppression, since the 180° RF pulse is selective in the SS-direction only.

Under off-resonance effects such as B_0 field inhomogeneities or susceptibility differences, the 2D excitation profile experiences a shift along the blipped SS-direction, which can also be calculated using Equation (5) with Δf corresponding to the off-resonance frequency this time. Since 2D RF pulses have long pulse durations, BW_{SS} is considerably smaller than that of a typical 180° RF pulse. Therefore, for a fixed Δf , the excitation profile of the 2D RF pulse experiences a considerably larger shift along the SS-direction when compared to that of the 180° RF pulse. The resulting mismatch between the excitation and refocusing profiles prevents complete refocusing of the excited slice, causing an effective loss of signal. This signal loss is position dependent due to the position dependence of Δf , causing an in-plane variability in the signal level. For fixed TBW_{SS} , longer 2D RF pulses have lower BW_{SS} , exhibiting increased off-resonance sensitivity. Note that while the 2D profile also shifts along the PE-direction, this shift is negligibly small and does not affect the mismatch with the refocusing profile, which acts along the SS-direction only.

Overall, Equations (4) and (5) show that robustness against off-resonance effects can be achieved only at the expense of reduced N_{max} or reduced T_{fast} , where the latter can only be achieved by reducing TBW_{PE} . Hence, standard 2D RF pulses exhibit a trade-off between off-resonance robustness versus slice coverage and/or slab profile sharpness.

2.2 | Sheared 2D echo-planar RF pulse design

Using a small tip angle approximation, the excitation profile of a 2D RF pulse can be written as:^{39,40}

$$M(z, y) = C_2(\alpha) \mathcal{F}^{-1} \{W(k_{SS}, k_{PE})S(k_{SS}, k_{PE})\}. \quad (6)$$

Here, z and y correspond to the SS- and PE-axes, respectively, \mathcal{F}^{-1} denotes inverse Fourier transformation. $C_2(\alpha)$ contains all scaling parameters to set the flip angle α , and S is the unit sampling function induced by the excitation k-space trajectory. For a standard 2D RF pulse, covering k_{PE} axis continuously and k_{SS} axis discretely, S can be expressed as a summation of line impulses:

$$S(k_{SS}, k_{PE}) = \sum_{n=-\infty}^{\infty} \delta(k_{SS} - n \Delta k_{SS}). \quad (7)$$

Using Equation (6), the excitation profile for a standard 2D RF pulse can then be derived as:

$$M(z, y) = \sum_{n=-\infty}^{\infty} w \left(\frac{z - n \Delta d_{SS}}{\Delta z}, \frac{y}{FOV_{PE}} \right), \quad (8)$$

where

$$w \left(\frac{z}{\Delta z}, \frac{y}{FOV_{PE}} \right) = \hat{C}_2(\alpha) \mathcal{F}^{-1} \{ W(k_{SS}, k_{PE}) \}. \quad (9)$$

Here, w denotes the desired 2D excitation profile (i.e., slice/slab thicknesses and sharpnesses) and $\hat{C}_2(\alpha) = C_2(\alpha) \Delta d_{SS}$ is a constant. Equation (8) confirms that the 2D excitation profile contains replicas along the SS-direction separated at Δd_{SS} distances, as previously given in Equation (3).

The slice coverage limitation can be removed if the replicas are pushed outside the slice stack along the SS-direction. To achieve this, we propose to cover the excitation k-space using a sheared trajectory, as shown in Figure 1A. For shearing with angle θ applied to k_{SS} axis, the sheared version of S can be expressed as a summation of sheared line impulses, that is,

$$\begin{aligned} S_{\text{shear}}(k_{SS}, k_{PE}) &= \frac{1}{|\cos(\theta)|} S(k_{SS} + k_{PE} \tan(\theta), k_{PE}) \\ &= \frac{1}{|\cos(\theta)|} \sum_{n=-\infty}^{\infty} \delta(k_{SS} + k_{PE} \tan(\theta) - n \Delta k_{SS}), \end{aligned} \quad (10)$$

where the scaling by $|\cos(\theta)|$ normalizes the sheared line impulses. Using Equation (6), the excitation profile for the sheared 2D RF pulse can then be derived as:

$$M_{\text{shear}}(z, y) = \sum_{n=-\infty}^{\infty} w \left(\frac{z - n \Delta d_{SS}}{\Delta z}, \frac{y - n \Delta d_{SS} \tan(\theta)}{FOV_{PE}} \right). \quad (11)$$

Accordingly, shearing does not change the profiles of the individual replicas, but only repositions them along the sheared axis, as displayed in Figure 2B. These replicas are separated at Δd_{SS} and $\Delta d_{SS} \tan(\theta)$ distances along the SS- and PE-directions, respectively, indicating that there is an angle θ between the sheared axis and the SS-axis. If the separation along the PE-direction is greater than FOV_{PE} , the replicas are completely pushed outside the slice stack, removing slice coverage limitations. The range of θ that satisfies this unlimited slice coverage criterion is:

$$\Delta d_{SS} \tan(\theta) \geq FOV_{PE}. \quad (12)$$

Using Equation (3), this criterion can be rewritten as:

$$\theta \geq \tan^{-1}(FOV_{PE} \Delta k_{SS}) = \tan^{-1} \left(\frac{FOV_{PE} TBW_{SS}}{N_{\text{blip}} \Delta z} \right). \quad (13)$$

For a desired 2D excitation profile, FOV_{PE} , TBW_{SS} , and Δz are all fixed. Hence, in theory, one can arbitrarily choose θ and compute the corresponding N_{blip} that guarantees unlimited slice coverage. According to Equation (13), choosing a large θ allows using a small N_{blip} , such that the excitation k-space can then be covered in fewer lines, resulting in reduced pulse duration. Note that the displacement between the fat and the water profiles is also repositioned along the sheared axis, such that the displacement along the SS-direction is still equal to Δd as expressed in Equation (5) and the displacement along the PE-direction is $\Delta d \tan(\theta)$. For fixed TBW_{SS} , reduced pulse duration yields increased BW_{SS} , which in turn provides off-resonance robustness at the expense of potentially incomplete fat suppression. Therefore, θ should be chosen small enough to ensure successful fat suppression.

Figure 1 shows an example case for sheared 2D RF pulse design. For a given θ , first N_{blip} and Δk_{SS} are computed. Then, the sheared trajectory that gives the corresponding S_{shear} within the hardware limits is obtained. As seen in Figure 1A, this “direct shearing” step yields an inefficient coverage of the excitation k-space: undesired coverage outside and missing coverage inside the targeted k-space extent will ultimately deteriorate the slice and slab profiles. Furthermore, the inefficiency of the coverage worsens with increasing θ . Therefore, we propose tailoring the sheared trajectory to obtain identical coverage as the standard trajectory, as shown in Figure 1A. In this tailored sheared trajectory, the corners of the targeted k-space extent are tucked in and filled by maintaining a fixed distance between the sheared trajectory lines. Note that the added lines do not alter the effective N_{blip} that determines the excitation profile, since $N_{\text{blip}} = K_{SS}/\Delta k_{SS}$ remains the same. Finally, the corresponding sheared 2D RF pulse can be computed using Equation (1). As shown in Figure 2, the replicas of the 2D excitation profile are along the SS-axis for the standard 2D RF pulses and along the sheared axis for the sheared 2D RF pulse. Likewise, the fat profiles demonstrate a large displacement from the water profile along the SS-axis for the standard 2D RF pulse and along the sheared axis for the sheared 2D RF pulse, enabling fat suppression using the 180° RF pulse of a spin echo sequence.

3 | METHODS

3.1 | 2D RF pulse design

MATLAB (MathWorks Inc.) was used for designing 2D RF pulses within the following hardware limits, based on the 3 T MRI scanner used in the experiments: $G_{\text{max}} = 28$ mT/m maximum gradient amplitude and $S_{\text{max}} = 150$

mT/m/ms maximum slew rate. Both RF and gradient waveforms were designed using $2 \mu\text{s}$ sampling time.

For a standard 2D RF pulse, first the gradient waveforms were designed directly within the hardware limits using the design parameters: $\text{FOV}_{\text{PE}} = 40 \text{ mm}$, $\Delta z = 4 \text{ mm}$, $\text{TBW}_{\text{PE}} = 8$, $\text{TBW}_{\text{SS}} = 3$, and $N_{\text{max}} = 16$. Next, the RF waveform was designed assuming a constant gradient amplitude for the echo-planar k-space trajectory. Then, following Equation (1), the RF waveform was scaled based on the time-varying gradient amplitudes using VERSE.⁴¹ The resulting standard 2D RF pulse was slew-rate limited and did not benefit from further pulse duration minimization via VERSE.⁴²

For a sheared 2D RF pulse at a given θ , first N_{blip} and Δk_{SS} were computed according to Equation (13). Then, the standard k-space trajectory was sheared using Equation (10) and the separation distances were rescaled to Δk_{SS} . After tailoring this sheared trajectory to match the coverage of the standard trajectory, the corresponding gradient waveforms were computed. Next, the RF waveform on the standard trajectory was interpolated to the sheared trajectory using scattered interpolation. Note that the shearing and separation adjustment operations can cause the hardware limits to be exceeded. Thus, VERSE was utilized to compute the minimum duration RF/gradient waveforms within the hardware limits with peak $B_1 = 15 \mu\text{T}$.⁴² Supporting information Figure S1 shows an example case before and after this VERSE step, where the pulse duration increases from 7.3 to 11.0 ms to enforce the hardware limits.

3.2 | Simulations

Simulations were performed in MATLAB to evaluate the performances of the 2D RF pulses. Fat profiles were simulated for $\Delta f = 440 \text{ Hz}$ at 3 T. For all simulations, T_1/T_2 relaxation effects were ignored when simulating the excitation profiles.

First, the duration and fat suppression capability of the sheared 2D RF design were evaluated as a function of θ . Based on the designed standard 2D RF pulse, sheared 2D RF pulses with θ ranging between 30° and 80° were generated, using the minimum N_{blip} that satisfies the unlimited slice coverage criterion in Equation (13) at each θ . Next, the ratio of the total fat signal and water signal in the 2D excitation profile after applying a 180° RF pulse was used as the performance metric for fat suppression. Here, we set the target fat/water signal ratio as 5%, that is, corresponding to a goal of 95% fat suppression. To compute their respective signals, the refocused fat and water profiles were integrated along the SS-axis (by incorporating through slice phase variations) at $\text{PE} = 0 \text{ mm}$. The

180° refocusing pulse was exported from the stock ssEPI sequence used in the MRI experiments, and was a standard three-lobe sinc-shaped RF pulse with 2.34 ms duration and $\text{BW}_{\text{SS}} = 1709 \text{ Hz}$.

Next, to analyze the effects of the design parameters on the sheared 2D RF pulse duration, each design parameter was varied while keeping other parameters fixed based on the parameters of the 16 ms standard 2D RF pulse given above. FOV_{PE} was varied between 30 and 60 mm, TBW_{PE} was varied between 6 and 10, Δz was varied between 3 and 5 mm, and TBW_{SS} was varied between 2 and 4. Furthermore, to investigate the effects of hardware limits, G_{max} was varied between 20 and 40 mT/m and S_{max} was varied between 100 and 200 mT/m/ms. For each parameter set, a standard 2D RF pulse and sheared 2D RF pulses with θ ranging between 30° and 80° were generated to demonstrate the trade-offs in sheared 2D RF design.

Finally, to quantitatively compare the off-resonance robustness performances of the standard and sheared 2D RF pulses, Bloch simulations were performed for off-resonance frequencies ranging between $\Delta f = \pm 160 \text{ Hz}$, that is, corresponding to $\pm 1.25 \text{ ppm}$ at 3 T. For each case, the center of mass for the main lobe of the 2D excitation profile before and after the 180° RF pulse was computed to quantify the off-resonance induced displacements. In addition, the in-plane signal level after the 180° RF pulse was evaluated as a function of off-resonance frequency and PE-position. At a given off-resonance frequency, the in-plane signal was computed by integrating the refocused 2D profile along the SS-axis, followed by a normalization with respect to the in-plane signal for $\Delta f = 0 \text{ Hz}$ and $\text{PE} = 0 \text{ mm}$. To quantify the improvement in off-resonance robustness achieved by the sheared 2D RF design, the signal ratios between sheared and standard 2D profiles were calculated as a function of off-resonance frequency and PE-position.

3.3 | MRI experiments

In vivo and phantom imaging experiments were conducted on a 3 T MRI scanner (Siemens Magnetom Trio) using an 8-channel spine array coil. In vivo imaging was conducted under the approval of the institutional review board. The stock ssEPI sequence was programmed in the IDEA pulse sequence programming environment to allow interchanging the excitation pulse between the following two options: (1) a standard 1D RF pulse preceded by an additional frequency-selective fat suppression RF pulse, or (2) a 2D RF pulse without any additional fat suppression. For these experiments, the standard and sheared 2D RF pulses featured in Figure 1 were utilized, where the standard 2D RF pulse had 16.0 ms duration and sheared 2D

RF pulse had 11.0 ms duration for $\theta = 63.25^\circ$. For both 2D RF pulses, the minimum dwell times of the MRI scanner were utilized, which were 2 μs for RF waveforms and 10 μs for gradient waveforms. The gradient waveforms were downsampled accordingly.

The phantom experiments were performed on a custom-built 1:1 scale head and neck phantom reflecting the anatomy of the brain and cervical spine.⁴³ In vivo experiments were conducted with three human subjects (two females, one male). For both the phantom and in vivo imaging experiments, the entire cervical spine region was covered via multislice T2-weighted ssEPI images acquired in the sagittal plane. For reduced-FOV imaging using the standard and sheared 2D RF pulses, the imaging parameters were: $200 \times 50 \text{ mm}^2$ FOV, 128×32 acquisition matrix. The echo time was $TE = 27 \text{ ms}$ and $TE = 22 \text{ ms}$ for the standard and sheared 2D RF pulse cases, respectively. Here, the 5 ms reduction in pulse duration allowed 5 ms reduction in TE for the sheared 2D RF pulse case. For full-FOV imaging using the one-dimensional (1D) RF pulse with additional fat suppression, the imaging parameters were: $200 \times 162.5 \text{ mm}^2$ FOV, 128×104 acquisition matrix, and $TE = 50 \text{ ms}$. Other imaging parameters were kept fixed between the reduced-FOV and full-FOV cases: $1.6 \times 1.6 \text{ mm}^2$ in-plane resolution, $\Delta z = 4 \text{ mm}$, 7 slices, $BW = 1860 \text{ Hz/Px}$, $TR = 6500 \text{ ms}$, $N_{\text{ave}} = 32$ (number of averages), and 6/8 partial Fourier acquisition.

Next, to quantitatively evaluate the off-resonance robustness of the 2D RF pulses, off-resonance field maps were acquired using a double-echo gradient echo (GRE) sequence with the following parameters: $TE_1 = 5.19 \text{ ms}$, $TE_2 = 7.65 \text{ ms}$, $1.2 \times 1.2 \text{ mm}^2$ in-plane resolution, $\Delta z = 4 \text{ mm}$, seven slices, $300 \times 300 \text{ mm}^2$ FOV, 256×256 acquisition matrix. The phase maps from the GRE sequence were phase unwrapped, and the off-resonance frequency maps were computed using the following relation:

$$\Delta f = \frac{\Delta\varphi}{2\pi\Delta TE}. \quad (14)$$

Here, $\Delta\varphi$ is the unwrapped phase and $\Delta TE = 2.46 \text{ ms}$ is the difference between TE_1 and TE_2 . Since this ΔTE corresponds to 2π phase difference for $\Delta f = 440 \text{ Hz}$, the resulting off-resonance map excluded the effects of chemical shift of fat. Note that the off-resonance map and ssEPI images do not align anatomically, since off-resonance causes a position-dependent shift (i.e., distortion) along the PE-direction in ssEPI images. This shift can be expressed as:⁴⁴

$$\Delta y = \Delta f T_{\text{ESP}} \text{FOV}_{\text{PE}}, \quad (15)$$

where T_{ESP} is ssEPI echo spacing. After compensating for this shift, Δf at all pixels in the ssEPI images were

determined using the off-resonance map. Next, pixel-wise signal ratios for the reduced-FOV images from the standard and sheared 2D RF cases were computed and plotted as a function of Δf at the corresponding pixels. These signal ratios were then compared with the theoretical signal ratios from simulations by taking into account the 5 ms difference in TE for the standard versus sheared 2D RF pulse cases. Here, the reduced TE further improves the signal ratio in favor of the sheared 2D RF pulse as follows: The agar-agar gel in the custom-built phantom was previously measured to have $T_2 = 61.9 \text{ ms}$,⁴³ corresponding to 1.084-fold improvement in signal ratio for 5 ms reduction in TE. Likewise, for the in vivo experiments, $T_2 = 73 \text{ ms}$ for white matter of the spinal cord⁴⁵ yields 1.071-fold improvement in signal ratio. Lastly, the theoretical signal ratios were multiplied by these additional improvements and compared with the pixel-wise signal ratios from the experiments.

4 | RESULTS

An example case comparing standard and sheared 2D RF pulses is demonstrated in Figure 1. Here, the standard 2D RF pulse has $N_{\text{blip}} = 40$, while the sheared 2D RF pulse has $\theta = 63.25^\circ$ with $N_{\text{blip}} = 14$. The corresponding RF and gradient waveforms are displayed in Figure 1B,C, where the resulting durations are 16.0 and 11.0 ms for the standard and sheared 2D RF pulses, respectively, providing 31.25% shortening of the pulse duration with the sheared design. Next, the corresponding 2D excitation profiles and 1D profiles along the PE- and SS-axes are shown in Figure 2, validating the fidelity of the slice and slab profiles for the sheared 2D RF design. For both 2D RF pulses, $\text{FOV}_{\text{PE}} = 40 \text{ mm}$, $\Delta z = 4 \text{ mm}$, $\text{TBW}_{\text{SS}} = 3$, and $\text{TBW}_{\text{PE}} = 8$. For the standard 2D RF pulse, the replicas are located along the SS-axis, limiting the slice coverage to $N_{\text{max}} = 16$. In contrast, the sheared 2D RF design positions the replicas along the sheared axis, providing unlimited slice coverage. In both cases, the fat profiles demonstrate a relative displacement with respect to the water profile, enabling fat suppression using a subsequent 180° RF pulse.

Figure 3 shows the duration and fat suppression capability of the sheared 2D RF pulse design as a function of θ for the same design parameters as in Figure 1. For a standard 2D RF pulse with 16 ms duration, Figure 3A shows 1D cross-sections along the SS-axis for water and fat profiles before and after the 180° RF pulse, in the absence of other off-resonance effects. As seen in this figure, the signal from fat is completely suppressed after the 180° RF pulse, yielding a fat/water signal ratio $< 0.02\%$. Figure 3B shows water and fat profiles for a sheared 2D RF pulse with $\theta = 63.25^\circ$ and 11.0 ms pulse duration. For fixed TBW_{SS} ,

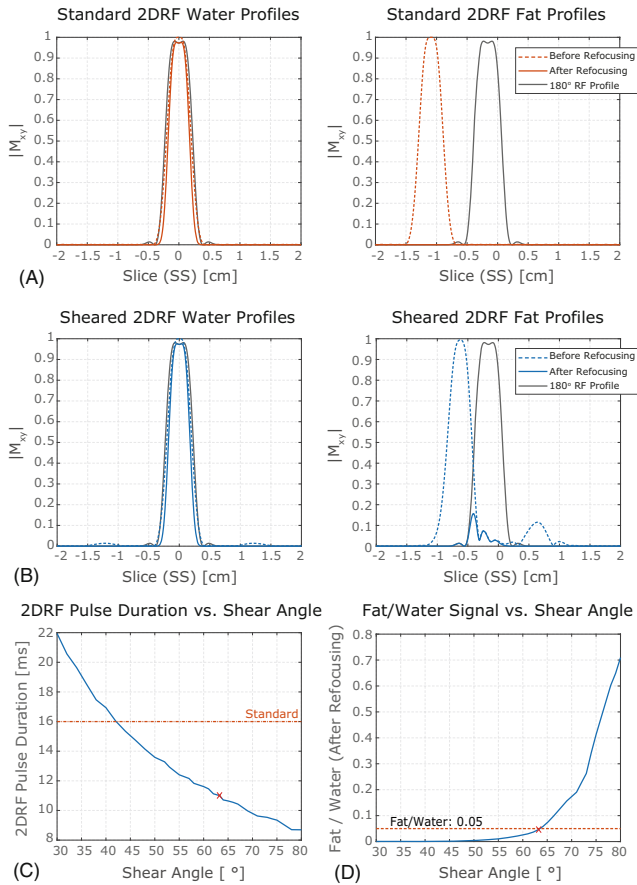


FIGURE 3 The durations and fat suppression capabilities of standard and sheared two-dimensional radiofrequency (2D RF) pulses as a function of θ . One-dimensional cross-sections of water and fat profiles along the slice-selection (SS)-axis for (A) the standard 2D RF pulse and (B) the sheared 2D RF pulse with $\theta = 63.25^\circ$ (i.e., the pulses in Figure 1), before and after the 180° refocusing RF pulse. Water and fat profiles for the 180° RF pulse are also shown (gray lines). While the signal from fat is completely suppressed for the standard design, a residual fat signal corresponding to an effective fat/water signal ratio of 5% is refocused for the sheared design. (C) The pulse duration and (D) the fat/water signal ratio for the sheared 2D RF pulse as a function of θ ranging between 30° to 80° . The shortest sheared 2D RF pulse that provides a target fat/water ratio of 5% has optimal $\theta = 63.25^\circ$ with 11.0 ms duration (red crosses). The design parameters were identical to those in Figure 1.

the reduced pulse duration causes an increase in BW_{SS} , resulting in a slight overlap of fat profiles for the sheared 2D RF pulse and the 180° RF pulse. For this case, the fat/water signal ratio was computed as 5%. This analysis was repeated for θ ranging between 30° and 80° . As seen in Figure 3C, the sheared 2D RF pulse duration decreases steadily as a function of θ , with $\theta > 42^\circ$ yielding pulses shorter than the standard 2D RF pulse. On the other hand, Figure 3D shows that the fat/water signal ratio remains relatively low for small θ , but increases rapidly for $\theta >$

65° . When evaluated together, the results in Figure 3C,D clearly display the trade-offs in the sheared design: a small θ causes the pulse duration to increase as it requires large N_{blip} to satisfy the unlimited slice coverage criterion (see Equation 13), whereas a large θ jeopardizes the fat suppression capability due to increased BW_{SS} . Setting a target fat/water signal ratio of 5% enables us to choose an optimal θ . Accordingly, for the given set of design parameters, the shortest sheared 2D RF pulse that satisfies the 5% target has optimal $\theta = 63.25^\circ$ with 11.0 ms duration (i.e., the case featured in Figure 3B).

The effects of design parameters and hardware limits on the sheared 2D RF pulse duration are shown in Figure 4, together with the corresponding standard 2D RF pulse durations. According to Figure 4A, while decreasing FOV_{PE} increases the standard 2D RF pulse duration, it decreases the sheared 2D RF pulse duration. The former result is consistent with Equation (2), where smaller FOV_{PE} requires an increase in K_{PE} for fixed TBW_{PE} , which in turn extends the k-space coverage and increases the pulse duration. In contrast, for the sheared 2D RF pulse, Equation (13) shows that smaller FOV_{PE} results in reduced N_{blip} for a fixed θ . This effect outweighs the former one and results in reduced pulse duration for the sheared 2D RF pulse. For both standard and sheared 2D RF pulses, the pulse duration increases with increasing TBW_{PE} . This result is consistent with Equation (2), since an increase in TBW_{PE} requires an increase K_{PE} . Figure 4B shows that while Δz has a negligible effect on the standard 2D RF pulse duration, the sheared 2D RF pulse duration increases with decreasing Δz . While Equation (2) shows that a decrease in Δz requires an increase in K_{SS} , this can easily be achieved for the standard 2D RF pulse by increasing the area under each gradient blip, without changing N_{blip} or the pulse duration. In contrast, for the sheared 2D RF pulse, Equation (13) shows that a decrease in Δz requires an increase in N_{blip} for a fixed θ , which in turn increases the pulse duration. For both standard and sheared 2D RF pulses, the pulse duration increases with increasing TBW_{SS} . This can be confirmed using Equation (4) for the standard 2D RF pulse, where an increase in TBW_{SS} requires an increase in N_{blip} for fixed N_{max} . Likewise, for the sheared 2D RF pulse, Equation (13) shows that larger TBW_{SS} requires a larger N_{blip} for a fixed θ . As shown in Figure 4C, G_{max} has a minimal effect on both the standard and sheared 2D RF durations, apart from a slight increase in sheared 2D RF pulse duration at low G_{max} . In contrast, decreasing S_{max} increases both the standard and sheared 2D RF durations. Note that these results are consistent with Figure 1B,C, where the gradient waveforms are dominated by the slew rate limits. Overall, these results demonstrate that the shearing operation generates 2D RF pulses with considerably reduced durations for a

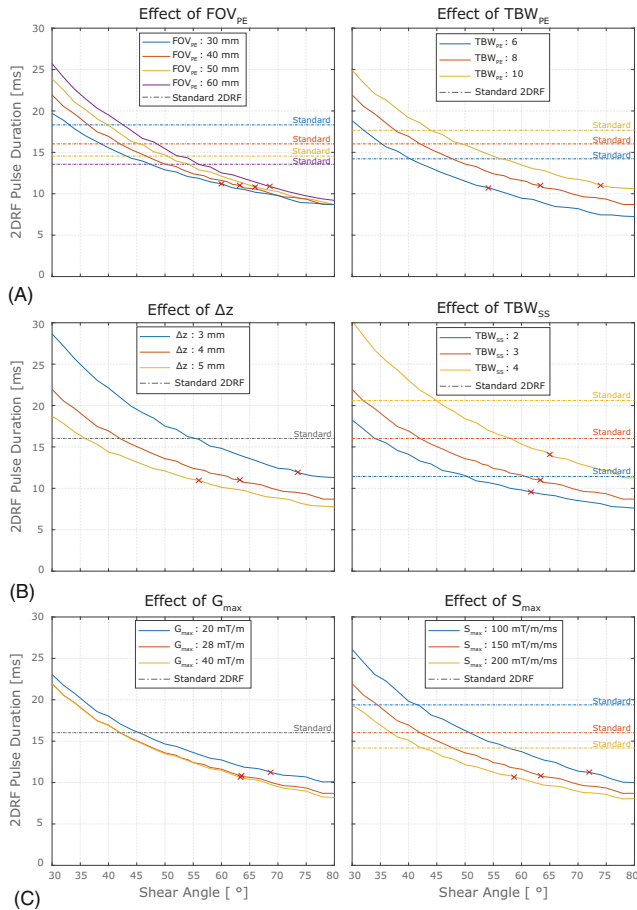


FIGURE 4 The effects of the design parameters and hardware limits on the pulse duration as a function of θ . (A) A decrease in FOV_{PE} increases the standard two-dimensional radiofrequency (2D RF) pulse duration (dashed lines), while it decreases the sheared 2D RF pulse duration. Increasing TBW_{PE} increases both the standard and sheared 2D RF pulse durations. (B) The standard 2D RF pulse duration is unaffected from Δz (as shown in gray dashed line for all Δz), whereas the sheared 2D RF pulse duration increases with decreasing Δz . An increase in TBW_{SS} increases both the standard and sheared 2D RF pulse durations. (C) Pulse durations are minimally affected by G_{max} but increase with decreasing S_{max} for both the standard and sheared 2D RF pulses. Overall, the sheared design generates pulses with considerably reduced durations. The red crosses indicate the sheared 2D RF pulses with optimal θ that satisfies the target fat/water signal ratio of 5%. Each parameter was varied while keeping others fixed, with default values of $FOV_{PE} = 40$ mm, $TBW_{PE} = 8$, $\Delta z = 4$ mm, $TBW_{SS} = 3$, $G_{max} = 28$ mT/m, and $S_{max} = 150$ mT/m/ms. For the standard 2D RF pulse, $N_{max} = 16$.

wide range of θ . For the parameters considered here, the optimal θ that satisfies the target fat/water signal ratio of 5% varies between 54° and 74° (marked with red crosses in Figure 4). Note that for the cases where $TBW_{SS} = 3$ was kept fixed (i.e., all results in Figure 4 except for the analysis on TBW_{SS}), the optimal θ corresponds to pulse durations around 11 ms. For larger TBW_{SS} , the optimal θ is reached

at longer pulse durations. These results are consistent with Equation (5), where targeting specific fat profile displacement (analogous to targeting a specific fat/water signal ratio) is equivalent to fixing BW_{SS} .

Off-resonance robustnesses of the standard and sheared 2D RF pulses are compared in Figure 5. In Figure 5A,B, the 2D profiles of the standard and sheared 2D RF pulses before and after the 180° refocusing RF pulse are displayed for on-resonance and $\Delta f = 64$ Hz off-resonance cases. As expected, the 2D standard and sheared profiles are almost identical for the on-resonance case, both before and after refocusing. In contrast, for $\Delta f = 64$ Hz case, the 2D profiles before refocusing demonstrate that the sheared 2D profile experiences a visibly reduced shift along the SS-direction due to its shorter pulse duration (i.e., larger BW_{SS}) when compared to the standard 2D profile. Comparing the 2D profiles after refocusing at $\Delta f = 64$ Hz, the effective slice for the sheared 2D profile exhibits only a minimal signal loss due to partial refocusing effects and is visibly thicker than the standard 2D profile. Next, Figure 5C demonstrates the off-resonance induced displacements in the center of mass for the main lobe of the 2D profiles before and after refocusing, for off-resonance frequency ranging between $\Delta f = \pm 160$ Hz. While the displacement for the standard 2D profile is mainly along the SS-direction with a negligibly small shift along the PE-direction, the sheared 2D profile displaces along both the SS- and PE-directions (i.e., along the sheared axis), as expected. Note that the displacement of the sheared 2D profile along the PE-direction is relatively small when compared to FOV_{PE} , and would therefore not induce a major problem during imaging. In contrast, the reduction in the displacement along the SS-direction is significant when compared to Δz , highlighting the off-resonance robustness achieved by the sheared 2D RF design.

Next, Figure 6 compares the in-plane signal levels for the standard and sheared 2D RF pulses as a function of off-resonance frequency and PE-position. These comparisons ignore relaxation effects to highlight the differences stemming from the excitation profiles alone. The signal level for the standard 2D RF pulse rapidly decreases with increasing off-resonance frequency, whereas the sheared 2D RF pulse maintains a high signal level for a wide range of off-resonance frequencies. For example, at $\Delta f = \pm 128$ Hz and $PE = 0$ mm, the signal levels are 0.82 and 0.48 for the sheared and standard 2D RF pulses, respectively, yielding a signal ratio of 1.71 (i.e., 71% improvement in signal). However, for the sheared 2D profile, the displacement along the PE-direction shown in Figure 5C causes an asymmetry in signal level as a function of PE-position. The signal ratio between the sheared and standard 2D profiles as a function of off-resonance frequency and

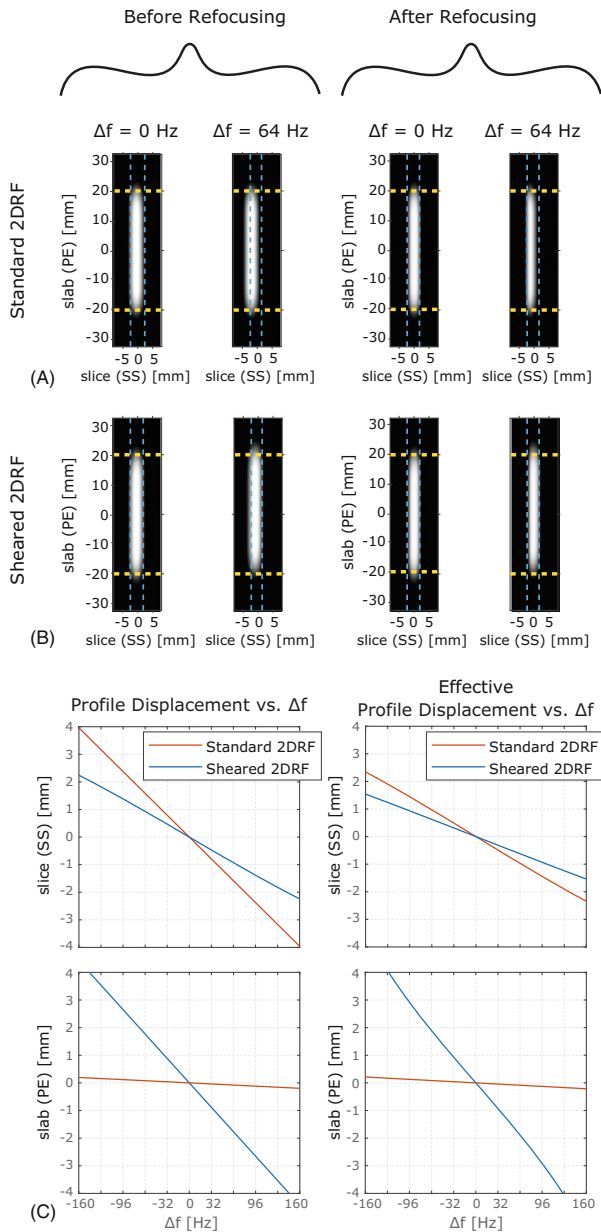


FIGURE 5 The comparison of off-resonance robustness for the standard and sheared two-dimensional radiofrequency (2D RF) pulses. The 2D profiles of (A) the standard and (B) the sheared 2D RF pulses before and after a 180° RF pulse for on-resonance and $\Delta f = 64$ Hz off-resonance cases. For reference, the borders of the targeted slab and slice thicknesses ($FOV_{PE} = 40$ mm and $\Delta z = 4$ mm) are marked with yellow and blue lines, respectively. The 2D profiles after refocusing are almost identical for the on-resonance case, whereas the effective slice for the sheared 2D RF pulse is visibly thicker for 64 Hz off-resonance case. (C) The profile displacements along the phase-encoding- and slice-selection (SS)-directions before and after refocusing under off-resonance ranging between $\Delta f = \pm 160$ Hz. The displacement is mainly along the SS-axis for the standard 2D RF pulse and along the sheared axis for the sheared 2D RF pulse. The displacement along the SS-direction is significantly reduced for the sheared 2D RF profile, highlighting its through-plane off-resonance robustness. The design parameters were identical to those in Figure 1.

PE-position is shown in Figure 6C. In the central $0.6FOV_{PE}$ region around the slab center, the sheared 2D RF pulse achieves increasing levels of signal ratio under increasing Δf . For off-central PE-positions, the signal ratio further increases in the proximity of the sheared axis. For PE-positions distant to the sheared axis, the signal level of the sheared 2D RF pulse is lower than its standard counterpart. Figure 6D provides a summary result for this position-dependent nature of the signal ratio, showing the median and 25th–75th percentiles for the signal ratio across the PE-direction as a function of Δf . Note that the distribution around the median is quite narrow and closely matches the signal ratio at PE = 0 mm, indicating that the aforementioned displacement of the sheared 2D profile along the PE-direction has a minor effect on the signal ratio. Importantly, the signal ratio exceeds 2 (i.e., 100% improvement in signal) for $|\Delta f| > 146$ Hz, highlighting the off-resonance robustness achieved by the sheared 2D RF design.

Figure 7 shows the phantom imaging results for the central slice of the sagittal slice stack. The GRE image in Figure 7A marks the graphical prescription of the full FOV and reduced FOV, and Figure 7E shows the off-resonance map from the double-echo GRE sequence. As seen in Figure 7B, off-resonance effects cause severe in-plane distortions in the full-FOV image acquired using a 1D RF pulse. In contrast, both of the reduced-FOV images in Figure 7C,D successfully alleviate these distortions and yield ssEPI images that depict the anatomy of the phantom more accurately. Furthermore, the sheared 2D RF pulse accomplishes substantial signal improvement in regions that exhibit high off-resonance, such as the upper cervical spine region (red arrows). Figure 7F compares the scatter plot of the experimental signal ratio with the theoretical signal ratio (with and without 5 ms TE difference taken into account), showing a close match between the two especially for the case where the TE difference is included. Here, the experimental signal ratio was computed for the reduced-FOV images from the sheared and standard 2D RF designs, and Δf for each pixel was determined using the off-resonance map after taking into account the distortion in PE-direction for ssEPI images (see Equation 15). To avoid background and signal pileup regions, only the pixels with intensities within 25%–67% of the maximum pixel intensity were utilized. Overall, the experimental results demonstrate a slightly higher signal ratio than expected theoretically. Importantly, the signal ratio is smaller than 1 for only 0.5% of pixels. In contrast, it exceeds 1.25 for 46.8% and 1.5 for 11.7% of pixels across the entire reduced FOV.

Finally, Figure 8A–E shows in vivo imaging results for Subject 1, covering the entire cervical spine sagittally. Again, both reduced-FOV images alleviate in-plane distortions when compared to the full-FOV image.

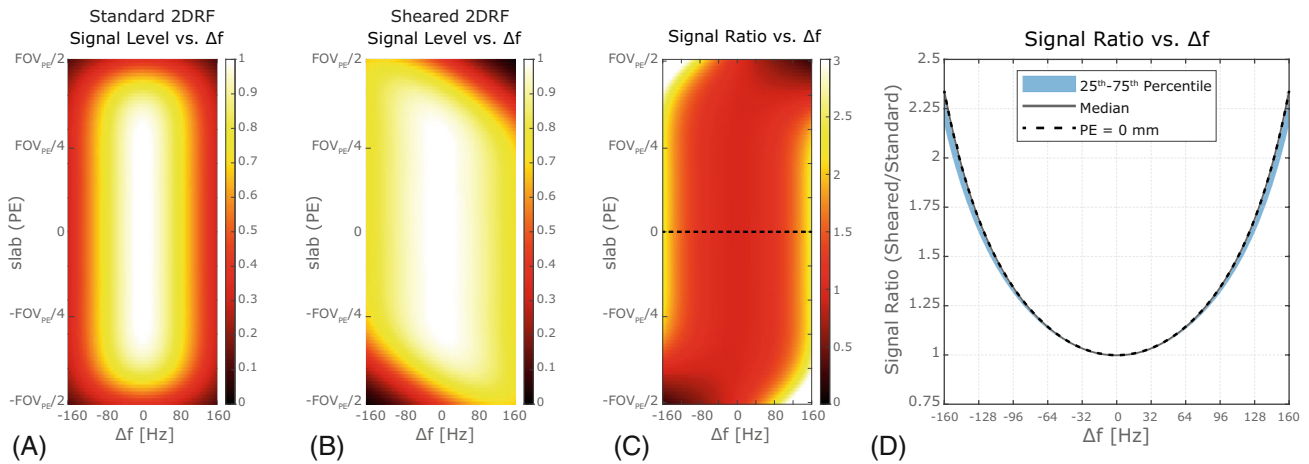


FIGURE 6 The in-plane signal levels for the standard and the sheared two-dimensional radiofrequency (2D RF) profiles as a function of off-resonance frequency and phase encoding (PE)-position. (A) For the standard case, the signal level is rapidly decreasing with increasing off-resonance. (B) The signal level for the sheared 2D RF pulse is preserved for a wide range of Δf , with an asymmetry along the PE-direction due to the profile displacement along the sheared axis. (C) The signal ratio between the sheared and standard 2D RF pulses as a function of off-resonance and PE-position. In the central $0.6\text{FOV}_{\text{PE}}$ region, the sheared 2D RF pulse achieves increasing levels of signal ratio for increasing Δf . Off-central PE-positions demonstrate even higher signal ratio in the proximity of the sheared axis. (D) The signal ratio (median and 25th–75th percentiles) across the PE-direction as a function of Δf . The distribution closely follows the signal ratio at PE = 0 mm (black dashed line). The design parameters were identical to those in Figure 1. These simulations ignored T_1/T_2 relaxation effects.

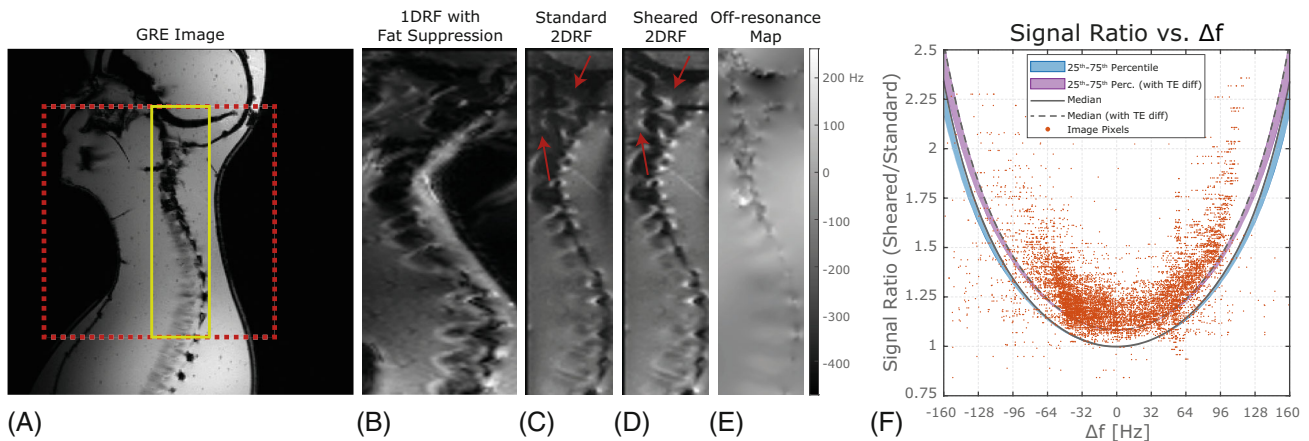


FIGURE 7 Phantom imaging results from the spine region of a custom-built head and neck phantom. (A) One of the gradient echo (GRE) images from the double-echo GRE sequence, with the prescribed full field-of-view (FOV; red dashed rectangle) and reduced-FOV (yellow rectangle) regions marked for reference. (B) The full-FOV image (cropped version shown), which was acquired using a one-dimensional radiofrequency (RF) pulse with additional frequency-selective fat suppression, suffers from severe in-plane distortions. The reduced-FOV images that were acquired using (C) the standard and (D) the sheared two-dimensional (2D) RF pulses accomplish high-resolution images with reduced in-plane distortions. The sheared 2D RF pulse substantially improves the signal levels, especially in regions exposed to high off-resonance (red arrows). (E) The off-resonance map obtained from the double-echo GRE sequence. (F) The experimental signal ratios (computed for the reduced-FOV images from the sheared and standard 2D RF pulses) are plotted together with the theoretical signal ratios (with and without the TE difference taken into account), showing a close match especially for the case where the TE difference is included. These results demonstrate that the sheared 2D RF pulse improves the signal level in the presence of off-resonance effects.

Furthermore, the sheared 2D RF design significantly improves the signal level in regions experiencing high off-resonance (see Figure 8E for off-resonance map), especially in the central cervical spine and upper thoracic spine

regions (red arrows). Detailed in vivo imaging results for Subject 2 and Subject 3 are provided in Supporting information Figure S2. For these two subjects, fat suppression during full-FOV imaging failed in lower cervical spine

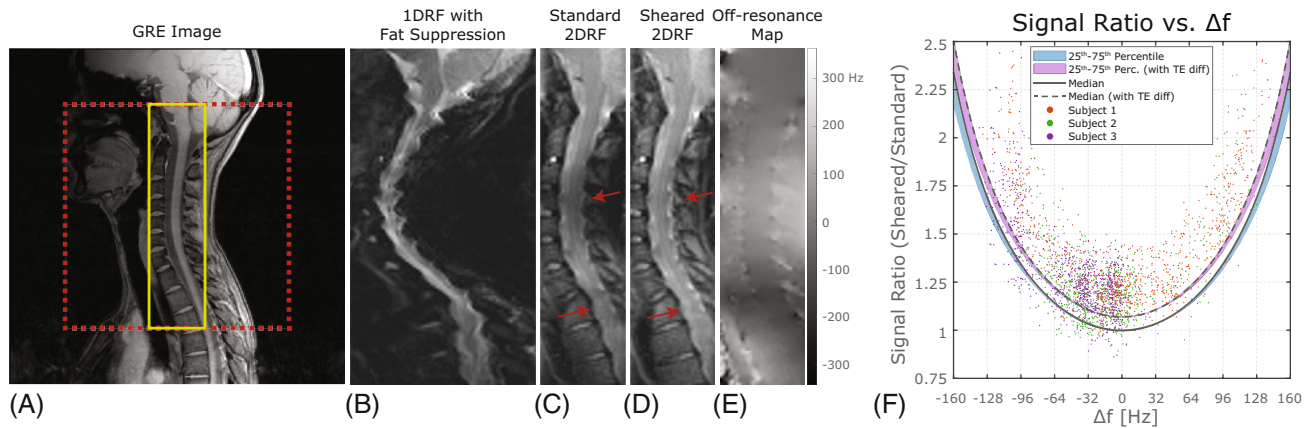


FIGURE 8 In vivo imaging results in the sagittal plane from the cervical spine of Subject 1 and signal ratio analysis for all three subjects. (A) One of the images from the double-echo gradient echo (GRE) sequence, showing the anatomy together with the full-field-of-view (FOV; red dashed rectangle), and reduced-FOV (yellow rectangle) regions marked for reference. (B) The full-FOV image (cropped version shown) suffers from severe in-plane off-resonance distortions. The reduced-FOV images with (C) the standard and (D) the sheared two-dimensional radiofrequency (2D RF) pulses alleviate these distortions and achieve high-resolution images. The sheared 2D RF pulse accomplishes remarkable signal improvement in regions exposed to high off-resonance (red arrows). (E) The off-resonance map from the double-echo GRE sequence. (F) The experimental signal ratios between the sheared and standard reduced-FOV images for all three subjects show a close agreement with the theoretical signal ratios (plotted with and without the TE difference taken into account), confirming the signal improvement achieved via the off-resonance robustness of the sheared design.

region, causing the displaced fat signal to overlap with and obscure the spinal cord. In contrast, both the standard and sheared 2D RF pulses demonstrate high fidelity fat suppression in addition to reduced in-plane distortions. Furthermore, the sheared 2D RF design shows higher signal levels in regions of high off-resonance. Figure 8F shows the signal ratio between the reduced-FOV in vivo images for all three subjects, in comparison to the theoretical signal ratio (with and without 5 ms TE difference taken into account). Here, the signal ratio was computed for pixels within ROIs manually drawn on the spinal cord region of each subject (see Supporting Information Figure S2 for ROIs). The in vivo results confirm the signal improvement achieved by the off-resonance robustness of the sheared 2D RF design. Similar to the case in the phantom imaging results, in vivo results exhibit a slightly higher signal ratio than expected. Across all subjects, the signal ratio is smaller than 1 for only 2.2% of pixels within ROIs. In contrast, it exceeds 1.25 for 53.2% and 1.5 for 21.3% of pixels within ROIs. These results emphasize that a large percentage of pixels within the spinal cord significantly benefit from the sheared 2D RF design, due to the abundance of off-resonance effects around the spine.

5 | DISCUSSION

In this work, we have proposed a sheared 2D RF pulse design that significantly reduces pulse durations and

provides robustness against through-plane off-resonance effects, while eliminating slice coverage limitations. Increasing the shear angle θ enables a reduction in the number of lines needed to cover the excitation k-space, which in turn reduces the pulse durations drastically while preserving the sharpness of the 2D excitation profile. According to Equation (5), the resulting increase in bandwidth decreases the separation between water and fat profiles, which may jeopardize fat suppression capability. Since unsuppressed fat signal experiences a large in-plane displacement in ssEPI sequences, inherent fat suppression is a highly desirable feature. Here, a target fat/water signal ratio of 5% was chosen as a design criterion, and the robustness of this approach was verified with reliable fat suppression demonstrated for in vivo imaging in the cervical spinal cord (see Supporting Information Figure S2).

The simulation results in Figure 4 confirm that the sheared 2D RF can successfully shorten the pulse duration for a wide range of design parameters, and that it becomes increasingly advantageous over the standard design as TBW_{PE} increases and FOV_{PE} decreases. This scenario corresponds to the case of a sharp slab profile over a small FOV_{PE} , that is, the typical scenario targeted with reduced-FOV applications. Furthermore, the sheared 2D RF design is highly effective in reducing pulse durations for typical hardware limits, and it becomes especially beneficial at reduced S_{max} . It should be noted that even for the cases where the reduction in pulse duration is relatively small, the sheared design still holds the advantage

of providing unlimited slice coverage, while preserving the fat suppression capability.

The through-plane off-resonance robustness achieved by the sheared 2D RF design was successfully demonstrated through extensive simulations, phantom experiments, and in vivo imaging experiments in the cervical spinal cord. The experimental results demonstrated a slightly higher signal ratio than expected, even after taking the TE difference into account. In this work, T_1/T_2 relaxation during RF pulses were ignored during theoretical computations. Therefore, the increased signal ratio in the experiments may reflect the added advantage of reduced relaxation effects for the sheared 2D RF pulse due to its shorter duration. In addition, signal pileup artifacts may also be a potential source, as multiple pixels experiencing different off-resonance frequencies may pile-up on to the same pixel in ssEPI images, making it difficult to resolve the true pixel intensities. Lastly, noise or deviations from the assumed T_2 value (especially for the in vivo case) may also be contributing factors to the observed variations.

The imaging experiments in this work were performed with the goal of highlighting the off-resonance robustness achieved via the sheared 2D RF design. The relatively large FOV in the sagittal plane and the large susceptibility differences around the cervical spine provided a suitable environment for this goal. Off-resonance frequencies reaching well above 128 Hz (>1 ppm) were observed, enabling experimental verification of the signal improvement achieved via the sheared design. In practice, imaging the spinal cord in the sagittal plane may complicate slice prescription, requiring oblique sagittal imaging. With that said, the axial plane is generally preferred for spinal cord imaging, as it can better resolve the fiber bundles in the cord.⁴⁶ However, imaging the spine in the axial plane requires a large number of slices, easily exceeding N_{\max} of a standard 2D RF pulse.²³ For those cases, the standard 2D RF pulse will experience partial saturation effects, causing the signal ratio to further increase in favor of the sheared 2D RF pulse. Note that if N_{\max} is exceeded, the fat profile of the standard 2D RF pulse would also experience partial saturation. However, because fat is already completely suppressed after the 180° RF pulse, partial saturation does not affect the fat signal. For the sheared 2D RF pulse, the replicas of the fat profile are shifted along the sheared axis with identical separation as that of the water profile replicas (see Figure 2B). Therefore, no partial saturation effect occurs for the sheared 2D RF pulse during multislice imaging.

Both the sheared and the standard 2D RF pulses were designed under identical hardware constraints and were optimized for minimal pulse duration. For the example shown in Figure 1, the reduction in pulse duration at a fixed flip angle caused the peak B_1 to increase from 10

μT to 15 μT for the sheared design. While 15 μT peak B_1 is within the hardware limits for MRI scanners, the specific absorption rate (SAR) for the sheared 2D RF pulse is 64% higher than its standard counterpart for this case. As a reference, the default excitation of the stock ssEPI sequence contained a standard 1D RF pulse with a peak B_1 of 7.2 μT preceded by a frequency-selective fat suppression RF pulse with a peak B_1 of 2.9 μT . When compared to this default excitation, the SAR of the sheared 2D RF pulse was 22% higher, whereas that of the standard 2D RF pulse was 26% lower. Considering the in-plane and through-plane off-resonance robustness provided by the sheared 2D RF pulse, the slight increase in SAR is tolerable. Note that the reported SAR values are highly dependent on the pulse durations (and hence the peak B_1 and gradient limits), as well as the specific design parameters for the 2D RF pulse. In the cases where the sheared design is more effective in reducing pulse durations (e.g., at reduced S_{\max}), the relative increase in SAR with respect to the standard 2D RF pulse will become more significant. Nonetheless, since ssEPI sequences utilize long TRs (typically TR > 3000 ms), the increase in SAR for the sheared 2D RF pulse is not expected to be a limiting factor.

The proposed sheared 2D RF pulse features a common design goal as that of the tilted 2D RF pulse:²³ positioning the replicas outside the slice stack to provide unlimited slice coverage. Because rotation and shearing are fundamentally different operations, the angle θ that guarantees unlimited slice coverage is different for the two cases: the equation for the tilt angle θ has an arcsine relation, whereas the shear angle θ has an arc-tangent relation with respect to the same parameters. The tilted design rotates the k-space trajectory by the tilt angle θ , without altering N_{blip} or Δk_{SS} . As a result, the tilted design does not achieve any pulse duration reduction and has minimal off-resonance robustness advantage over the standard 2D RF pulse.²³ Furthermore, rotation causes poor coverage of the targeted k-space extent, causing degradation in 2D profile quality. In contrast, the sheared 2D RF design minimizes N_{blip} and maximizes Δk_{SS} for a given shear angle θ , achieving significant reductions in the pulse duration. Note that one could decrease N_{blip} and increase Δk_{SS} to reduce the tilted 2D RF pulse duration, as well. However, making N_{blip} smaller would cause the tilt angle θ to increase, which would further exacerbate the poor k-space coverage problem, causing severe degradations in the 2D profile. A related work proposed starting from a square echo-planar trajectory, followed by rotation and scaling to better cover a rectangular k-space extent.⁴⁷ While the resulting tilted trajectory overcame some of the aforementioned poor k-space coverage issues, it still did not cover the entirety of the targeted

k-space extent and hence is prone to 2D profile degradations. In contrast, even direct shearing of the trajectory provides good coverage of the targeted k-space. The proposed tailoring of the sheared trajectory achieves identical coverage as the standard trajectory, preserving 2D profile quality. While the standard 2D RF pulse duration could also be reduced by decreasing N_{blip} , doing so would increase partial saturation effects during multislice acquisitions. Alternatively, N_{blip} and TBW_{SS} could be decreased at the same rate to keep N_{max} constant, which in turn would degrade the slice profile. Nonetheless, the sheared design can provide further reduction in pulse durations even for small TBW_{SS} cases (see Figure 4B), with the added advantage of unlimited slice coverage. Moreover, Figure 4 demonstrates that the sheared design also provides a flexibility while choosing θ for a given 2D profile. Consequently, pulse durations could be further shortened by increasing θ , forsaking the fat suppression performance in favor of further improvement in off-resonance robustness. In such a case, an external fat suppression method can be incorporated, such as a frequency-selective fat suppression RF pulse or a short tau inversion recovery.

In this work, the blipped direction for the standard 2D RF pulse was the SS-axis. An alternative design is to assign the PE-axis as the blipped direction,²⁸ which requires large N_{blip} or small TBW_{PE} to prevent aliasing artifacts due to the replicas along the PE-direction. Note that aliasing is a considerably more severe problem than the above-mentioned signal loss due to partial saturation effect. To avoid aliasing, a tilted alternative was proposed to rotate the k-space trajectory by a relatively small tilt angle θ , such that a subsequent 180° RF pulse can suppress the replicas.³⁶ However, both the original and tilted designs require additional fat suppression and have reduced slab sharpness due to the need for small TBW_{PE} , an undesirable feature for reduced-FOV imaging. Another alternative approach for reduced-FOV imaging is to utilize 2D spatially selective excitation with a spiral trajectory,³⁹ which provides relatively short pulse durations especially after applying a variable slew-rate spiral trajectory.⁴⁸ However, spiral RF pulse is more suited for circular 2D excitation profiles, as it lacks the flexibility of independent design along the SS- and PE-axis. In contrast, the proposed sheared 2D RF pulse provides sharp slab and slice profiles, with unlimited slice coverage and inherent fat suppression capability.

6 | CONCLUSION


In this work, we have proposed a sheared 2D RF pulse design to achieve robustness against through-plane off-resonance effects via a significant reduction in pulse

duration. This technique eliminates slice coverage limitations, while maintaining profile sharpness and high fidelity fat suppression. The performance of the proposed technique was demonstrated in the cervical spine, showing significant signal improvements in regions exposed to off-resonance effects. While the results were demonstrated for ssEPI images, this design can be applied for reduced-FOV imaging for spin echo sequences with any acquisition type. The proposed sheared 2D RF approach will be especially beneficial in regions that suffer from large off-resonance effects, such as spinal cord and breast.


ACKNOWLEDGMENTS

This work was supported by the Scientific and Technological Research Council of Turkey (TUBITAK Grant No: 117E116). Parts of this work were presented at the 2021 Annual Meeting of ISMRM.

ORCID

Bahadır Alp Barlas  <https://orcid.org/0000-0001-6963-9644>

Cagla Deniz Bahadır  <https://orcid.org/0000-0003-2247-9975>

Sevgi Gokce Kafali  <https://orcid.org/0000-0001-5941-5399>

Emine Ulku Saritas  <https://orcid.org/0000-0001-8551-1077>

REFERENCES

1. Reeder S, Mujherjee P. Clinical applications of MR diffusion and perfusion imaging. *Magn Reson Imaging Clin N Am*. 2009;17:xi-xii.
2. Holdsworth S, O'Halloran R, Setsompop K. The quest for high spatial resolution diffusion-weighted imaging of the human brain in vivo. *NMR Biomed*. 2019;32:e4056.
3. Brazzelli M, Sandercock P, Chappell F, et al. Magnetic resonance imaging versus computed tomography for detection of acute vascular lesions in patients presenting with stroke symptoms. *Cochrane Database Syst Rev*. 2009;CD007424.
4. Barentsz J, Richenberg J, Clements R, et al. ESUR prostate MR guidelines 2012. *Eur Radiol*. 2012;22:746-757.
5. Bhat S, Fernandes T, Poojar P, et al. Low-Field MRI of stroke: challenges and opportunities. *J Magn Reson Imaging*. 2021;54:372-390.
6. Zaharchuk G, Saritas E, Andre J, et al. Reduced field-of-view diffusion imaging of the human spinal cord: comparison with conventional single-shot echo-planar imaging. *AJNR Am J Neuroradiol*. 2011;32:813-820.
7. Dietrich O, Biffar A, Baur-Melnyk A, Reiser M. Technical aspects of MR diffusion imaging of the body. *Eur J Radiol*. 2010;76:314-322.
8. Singer L, Wilmes L, Saritas E, et al. High-resolution diffusion-weighted magnetic resonance imaging in patients with locally advanced breast cancer. *Acad Radiol*. 2012;19:526-534.

9. Korn N, Kurhanewicz J, Banerjee S, Starobinets O, Saritas E, Noworolski S. Reduced-FOV excitation decreases susceptibility artifact in diffusion-weighted MRI with endorectal coil for prostate cancer detection. *Magn Reson Imaging*. 2015;33:56-62.
10. Leibfarth S, Winter R, Lyng H, Zips D, Thorwarth D. Potentials and challenges of diffusion-weighted magnetic resonance imaging in radiotherapy. *Clin Transl Radiat Oncol*. 2018;13:29-37.
11. An H, Ma X, Pan Z, Guo H, Lee E. Qualitative and quantitative comparison of image quality between single-shot echo-planar and interleaved multi-shot echo-planar diffusion-weighted imaging in female pelvis. *Eur Radiol*. 2020;30:1876-1884.
12. Tournier J, Mori S, Leemans A. Diffusion tensor imaging and beyond. *Magn Reson Med*. 2011;65:1532-1556.
13. Holdsworth S, Skare S, Newbould R, Guzman R, Blevins N, Bammer R. Readout-segmented EPI for rapid high resolution diffusion imaging at 3 T. *Eur J Radiol*. 2008;65:36-46.
14. Holdsworth S, Skare S, Newbould R, Bammer R. Robust GRAPPA-accelerated diffusion-weighted readout-segmented (RS)-EPI. *Magn Reson Med*. 2009;62:1629-1640.
15. Heidemann R, Porter D, Anwender A, Feiweier T, Knösche T, Turner R. Diffusion imaging in humans at 7T using readout-segmented EPI and GRAPPA. *Magn Reson Med*. 2010;64:9-14.
16. Skare S, Newbould R, Nordell A, Holdsworth S, Bammer R. An auto-calibrated, angularly continuous, two-dimensional GRAPPA kernel for propeller trajectories. *Magn Reson Med*. 2008;60:1457-1465.
17. Guhaniyogi S, Chu M, Chang H, Song A, Chen N. Motion immune diffusion imaging using augmented MUSE for high-resolution multi-shot EPI. *Magn Reson Med*. 2016;75:639-652.
18. Liu W, Zhao X, Ma Y, Tang X, Gao J. DWI using navigated interleaved multishot EPI with realigned GRAPPA reconstruction. *Magn Reson Med*. 2016;75:280-286.
19. Dong Z, Wang F, Ma X, et al. Interleaved EPI diffusion imaging using SPIRiT-based reconstruction with virtual coil compression. *Magn Reson Med*. 2018;79:1525-1531.
20. Feinberg D, Hoenninger J, Crooks L, Kaufman L, Watts J, Arakawa M. Inner volume MR imaging: technical concepts and their application. *Radiology*. 1985;156:743-747.
21. Wilm B, Svensson J, Henning A, Pruessmann K, Boesiger P, Kollias S. Reduced field-of-view MRI using outer volume suppression for spinal cord diffusion imaging. *Magn Reson Med*. 2007;57:625-630.
22. Saritas E, Cunningham C, Lee J, Han E, Nishimura D. DWI of the spinal cord with reduced FOV single-shot EPI. *Magn Reson Med*. 2008;60:468-473.
23. Banerjee S, Nishimura D, Shankaranarayanan A, Saritas E. Reduced field-of-view DWI with robust fat suppression and unrestricted slice coverage using tilted 2D RF excitation. *Magn Reson Med*. 2016;76:1668-1676.
24. Heidemann R, Anwender A, Feiweier T, Knösche T, Turner R. k-space and q-space: combining ultra-high spatial and angular resolution in diffusion imaging using ZOOPPA at 7 T. *Neuroimage*. 2012;60:967-978.
25. Wargo C, Gore J. Localized high-resolution DTI of the human midbrain using single-shot EPI, parallel imaging, and outer-volume suppression at 7T. *Magn Reson Imaging*. 2013;31:810-819.
26. Wheeler-Kingshott C, Hickman S, Parker G, et al. Investigating cervical spinal cord structure using axial diffusion tensor imaging. *Neuroimage*. 2002;16:93-102.
27. Dowell N, Jenkins T, Ciccarelli O, Miller D, Wheeler-Kingshott C. Contiguous-slice zonally oblique multi-slice (CO-ZOOM) diffusion tensor imaging: examples of in vivo spinal cord and optic nerve applications. *Magn Reson Imaging*. 2009;29:454-460.
28. Finsterbusch J. High-resolution diffusion tensor imaging with inner field-of-view EPI. *J Magn Reson Imaging*. 2009;29:987-993.
29. Wilm B, Gamper U, Henning A, Pruessmann K, Kollias S, Boesiger P. Diffusion-weighted imaging of the entire spinal cord. *NMR Biomed*. 2009;22:174-181.
30. Andre J, Zaharchuk G, Saritas E, et al. Clinical evaluation of reduced field-of-view diffusion-weighted imaging of the cervical and thoracic spine and spinal cord. *AJNR Am J Neuroradiol*. 2012;33:1860-1866.
31. Wilmes L, McLaughlin R, Newitt D, et al. High-resolution diffusion-weighted imaging for monitoring breast cancer treatment response. *Acad Radiol*. 2013;20:581-589.
32. Zhang Y, Holmes J, Rabanillo I, Guidon A, Wells S, Hernando D. Quantitative diffusion MRI using reduced field-of-view and multi-shot acquisition techniques: validation in phantoms and prostate imaging. *Magn Reson Imaging*. 2018;51:173-181.
33. Schneider R, Ritter D, Haueisen J, Pfeuffer J. B0-informed variable density trajectory design for enhanced correction of off-resonance effects in parallel transmission. *Magn Reson Med*. 2014;71:1381-1393.
34. Ma C, Xu D, King K, Liang Z. Reduced field-of-view excitation using second-order gradients and spatial-spectral radiofrequency pulses. *Magn Reson Med*. 2013;69:503-508.
35. Islam H, Glover G. Reduced field of view imaging using a static second-order gradient for functional MRI applications. *Magn Reson Med*. 2016;75:817-822.
36. Finsterbusch J. Improving the performance of diffusion-weighted inner field-of-view echo-planar imaging based on 2D-selective radiofrequency excitations by tilting the excitation plane. *J Magn Reson Imaging*. 2012;35:984-992.
37. Lee E, Hwang J, Chang Y, et al. Modified reduced field-of-view diffusion-weighted magnetic resonance imaging of the prostate: comparison with reduced field-of-view imaging and single shot echo-planar imaging. *J Comput Assist Tomogr*. 2021;45:367-373.
38. Tanabe M, Higashi M, Benkert T, et al. Reduced field-of-view diffusion-weighted magnetic resonance imaging of the pancreas with tilted excitation plane: a preliminary study. *J Magn Reson Imaging*. 2021;54:715-720.
39. Pauly J, Nishimura D, Macovski A. A k-space analysis of small-tip-angle excitation. *J Magn Reson*. 1989;81:43-56.
40. Alley M, Pauly J, Sommer F, Pelc N. Angiographic imaging with 2D RF pulses. *Magn Reson Med*. 1997;37:260-267.
41. Conolly S, Nishimura D, Macovski A, Glover G. Variable-rate selective excitation. *J Magn Reson*. 1988;78:440-458.
42. Lee D, Lustig M, Grissom W, Pauly J. Time-optimal design for multidimensional and parallel transmit variable-rate selective excitation. *Magn Reson Med*. 2009;61:1471-1479.
43. Aygun E, Cagil R, Saritas E. 1-1 scale agar-agar paramagnetic phantom for brain and cervical spine MRI. Proceedings of the 2021 Annual Meeting of ISMRM; 2021:3355.

44. Jezzard P, Balaban R. Correction for geometric distortion in echo planar images from B0 field variations. *Magn Reson Med.* 1995;34:65-73.
45. Smith S, Edden R, Farrell J, Barker P, Zijl PV. Measurement of T_1 and T_2 in the cervical spinal cord at 3 tesla. *Magn Reson Med.* 2008;60:213-219.
46. Stroman P, Wheeler-Kingshott C, Bacon M, et al. The current state-of-art of spinal cord imaging: methods. *Neuroimage.* 2014;84:1070-1081.
47. Zhong Z, Merkitich D, Karaman M, et al. High-spatial-resolution diffusion MRI in Parkinson disease: lateral asymmetry of the Substantia Nigra. *Radiology.* 2019;291:149-157.
48. Xu D, King K, Liang Z. Variable slew-rate spiral design: theory and application to peak B1 amplitude reduction in 2D RF pulse design. *Magn Reson Med.* 2007;58:835-842.

SUPPORTING INFORMATION

Additional supporting information may be found in the online version of the article at the publisher's website.

Figure S1 The sheared two-dimensional radiofrequency (2D RF) pulse from Figure 1, before and after applying VERSE to generate the minimum duration pulse within the hardware limits ($G_{\max} = 28$ mT/m, $S_{\max} = 150$ mT/m/ms, peak $B_1 = 15$ μ T). The pulse before VERSE significantly exceeds the hardware limits, as it was computed by shearing the k-space trajectory without any constraints. After applying VERSE, the pulse duration increases from 7.3 ms to 11.0 ms. This sheared 2D RF pulse is 31% shorter than its standard counterpart, which has 16.0 ms duration.

Figure S2 In vivo imaging results in the cervical spine for all subjects. (A) Subject 1, (B) Subject 2, and (C) Subject 3. The images from the double-echo GRE sequences show the anatomy together with the full field-of-view (FOV; red dashed rectangle) and reduced-FOV (yellow rectangle) regions marked for reference. The full-FOV images

for all subjects (cropped versions shown), acquired using a 1D RF pulse with additional frequency-selective fat suppression, suffer from severe in-plane off-resonance distortions. Furthermore, displaced fat signals overlap with and obscure the spinal cord in the lower cervical spine region for Subjects 2 and 3 (yellow arrows), indicating that fat suppression has failed for these subjects. In contrast, both the standard and sheared 2D RF pulses demonstrate high fidelity fat suppression, as well as high image resolution and reduced in-plane distortions. In addition, the sheared 2D RF pulse achieves visible signal improvement over the standard 2D RF pulse, especially in regions that suffer from high off-resonance (red arrows). The signal levels of the images obtained from the sheared and standard 2D RF pulses were compared quantitatively using the pixels within manually drawn ROIs covering the spinal cord (solid red lines in the off-resonance maps). The experimental signal ratio matches closely with the theoretical signal ratio (plotted with and without the TE difference taken into account) for all three subjects. These results confirm the signal improvement achieved via the off-resonance robustness of the sheared 2D RF design.

How to cite this article: Barlas BA, Bahadir CD, Kafali SG, Yilmaz U, Saritas EU. Sheared two-dimensional radiofrequency excitation for off-resonance robustness and fat suppression in reduced field-of-view imaging. *Magn Reson Med.* 2022;88:2504-2519. doi: 10.1002/mrm.29416

WOULD YOU LIKE TO POST AN INFORMAL COMMENT ABOUT THIS PAPER, OR ASK THE AUTHORS A QUESTION ABOUT IT?

If so, please visit <https://mrm.ismrm.org/> and register for our Magn Reson Med Discourse site (registration is free).

The screenshot shows the Magn Reson Med Discourse website. At the top, there is a search bar and a navigation menu with 'all categories', 'Categories', 'Latest', and 'Top'. A '+ New Topic' button is also visible. The main content area is divided into three columns: 'Category', 'Topics', and 'Latest'. The 'Category' column lists 'MRM Papers' with a description and a grid of volume and issue options. The 'Topics' column shows '164' topics. The 'Latest' column displays three recent topics: '[April 2022] Reproducible Research Insights with Jakob Assländer', 'MRM Highlights Magazine - Volume 7', and '[April 2022] Q&A with Jakob Assländer and Daniel Sodickson'. Each topic includes a small icon, a title, a user profile picture, and a '0' comment count.

Magn Reson Med is currently listing the top 8 downloaded papers from each issue (including Editor's Picks) for comments and questions on the Discourse web site.

However, we are happy to list this or any other papers (please email mrm@ismrm.org to request the posting of any other papers.)

We encourage informal comment and discussion about Magn Reson Med papers on this site. Please note, however, that a formal errata from the authors should still be submitted in the usual way via our Manuscript Central online submission system.